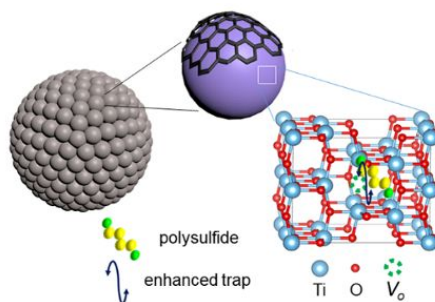




Oxygen-deficient titanium dioxide as a functional host for lithium-sulfur batteries

Journal:	<i>Journal of Materials Chemistry A</i>
Manuscript ID	TA-ART-02-2019-001598.R1
Article Type:	Paper
Date Submitted by the Author:	11-Mar-2019
Complete List of Authors:	<p>Wang, Hong-En; Wuhan University of Technology, State Key Laboratory of Advanced Technology for Materials Synthesis and Processing; University of Washington, Materials Science and Engineering</p> <p>Yin, Kaili; Wuhan University of Technology, State Key Laboratory for Materials Synthesis and Processing</p> <p>Qin, Ning; Southern University of Science and Technology of China, Materials Science and Engineering</p> <p>Zhao, Xu; University of Washington, Materials Science and Engineering; Materials Science and Engineering</p> <p>Xia, Fan-Jie; Wuhan University of Technology</p> <p>Hu, Zhi-Yi; NRC (Nanostructure Research Centre) Wuhan University of Technology Wuhan, 122 Luoshi Road, 430074 (P.R. China)</p> <p>Guo, Guanlun; Hubei Key Laboratory of Advanced Technology for Automotive Components & Hubei Collaborative Innovation Center for Automotive Components Technology Wuhan University of Technology, school of automotive engineering</p> <p>Cao, Guozhong; University of Washington, Materials Science and Engineering</p> <p>Zhang, Wenjun; City University of Hong Kong, Department of Physics and Materials Science, and Center of Super-Diamond and Advanced Film</p>

Table of Contents



Engineering oxygen vacancies in mesoporous TiO₂ effectively enhanced its entrap to polysulfides and simultaneously propelled the redox conversion of polysulfides.

ARTICLE

Oxygen-deficient titanium dioxide as a functional host for lithium-sulfur batteries

Hong-En Wang,^a Kaili Yin,^a Ning Qin,^c Xu Zhao,^d Fan-Jie Xia,^a Zhi-Yi Hu,^a Guanlun Guo,^{*f} Guozhong Cao^{*e} and Wenjun Zhang^{*b}

Received 00th January 20xx,
Accepted 00th January 20xx

DOI: 10.1039/x0xx00000x

The shuttling of polysulfides with sluggish redox kinetics has severely retarded the advancement of lithium-sulfur (Li-S) batteries. In this work oxygen-deficient titanium dioxide (TiO₂) has been investigated as a novel functional host for Li-S batteries. Experimental and first-principles density functional theory (DFT) studies reveal that the oxygen vacancies (V_o^{**}) help to reduce the polysulfide shuttling and catalyze the redox kinetics of sulfur/polysulfides during cycling. Consequently, the resulting TiO₂/S composite cathode manifests superior electrochemical properties in terms of high capacity (1472 mA h g⁻¹ at 0.2 C), outstanding rate (571 mA h g⁻¹ at 2 C), and excellent cycling property (900 mA h g⁻¹ over 100 cycles at 0.2 C). The present strategy offers a viable way through vacancy engineering for design and optimization of high-performance electrodes for advanced Li-S batteries and other electrochemical devices.

Introduction

Lithium-sulfur (Li-S) batteries (LSBs) have been considered as a promising next-generation electrochemical energy storage system due to their ultrahigh theoretical energy density (2600 W h kg⁻¹), abundant sulfur source in earth crust with low-cost, and environmental benignity.¹⁻³ However, the electrochemical performance of LSBs has been largely affected by the shuttling of lithium polysulfide intermediates (Li₂S_x, 3 < x ≤ 8) being dissoluble easily in ether-based electrolyte.⁴ Thus far, various approaches have been reported to address the intractable issue of polysulfide shuttling, e.g., through modifying separator,⁵ adding interlayers,^{6,7} optimizing binder^{8,9} and electrolyte composition,^{10,11} and manipulating Li-anodes to enhance their stability.¹² Nevertheless, due to the changing polarities of polysulfides during discharge/charge processes, these approaches could suppress their shuttling to a certain extent

only. There is still a considerable space for improving the performance of LSBs before they could be used practically.

Regulating the composition and structure of cathode is another useful strategy to tackle the problem of polysulfide shuttling.¹³⁻¹⁵ Particularly, cathodes based on various carbon nanostructures have been reported, such as meso-/microporous carbon,^{16,17} hollow carbon,^{18,19} graphene,²⁰ carbon nanotubes,^{20,21} and their composites.^{22, 23} In general, due to the intrinsically non-polar nature of these carbon materials, they could not mitigate the shuttling of polysulfides alone.^{24,25} Polar compounds, such as transitional metal oxides,²⁶⁻²⁹ sulfides,³⁰⁻³³ selenides,³⁴ carbides,³⁵ nitrides,³⁶⁻⁴¹ and phosphides,^{42,43} have thus drawn increasing attention as potential cathode hosts because of their stronger chemical affinity to polysulfides. Among these polar compounds, TiO₂ has manifested a high affinity to polysulfide due to strong Lewis acid-base interaction between the empty 3d orbitals of Ti⁴⁺ and electron-rich polysulfide anions (S_x²⁻).^{44,45} Moreover, TiO₂ could promote the redox conversion of polysulfides during charge/discharge.⁴⁶ However, the electrical conductivity of TiO₂ and its interaction with polysulfides need to be further improved for application in practical LSBs.

Hybridizing TiO₂ with graphene,^{47,48} carbon nanotubes⁴⁹, porous carbon matrix⁵⁰ or MXene⁵¹ enabled enhanced electric conductivity of TiO₂-based electrodes used in LSBs, albeit with multi-step and complicated processing were required, and uneven distribution of respective components in the final composites was another problem to be solved. Thus, rational design and fabrication of TiO₂/C composite with controlled composition and component distribution by facile reaction routes are still desired as sulfur hosts for high-performance LSBs. Alternatively, incorporation of oxygen vacancy (V_o^{**}) in TiO₂ has been proposed as an effective route to boost its electric conductivity as V_o^{**} can serve as a shallow donor to increase the

^a State Key Laboratory of Advanced Technology for Materials Synthesis and Processing, Wuhan University of Technology, Wuhan 430070, China.

^b Centre of Super Diamond & Advanced Films (COSDAF) and Department of Materials Science and Engineering, City University of Hong Kong, HKSAR, China. Email: apwjzh@cityu.edu.hk

^c Department of Materials Science and Engineering, Southern University of Science and Technology, Shenzhen 518055, China.

^d Institute of Chemical Materials, China Academy of Engineering Physics, Mianyang 621900, China.

^e Department of Materials Science and Engineering, University of Washington, Seattle, WA 98195, USA. Email: gzcao@u.washington.edu

^f Hubei Key Laboratory of Advanced Technology for Automotive Components, Wuhan University of Technology, Wuhan 430070, China. Email: glguo@whut.edu.cn

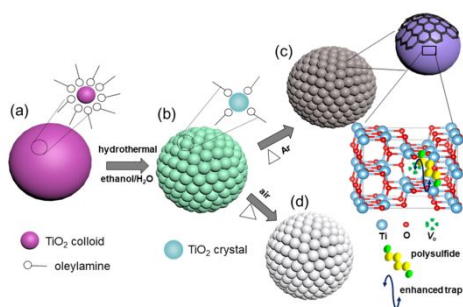
† Footnotes relating to the title and/or authors should appear here.

Electronic Supplementary Information (ESI) available: experimental section, scheme for materials synthesis, digital photos, SEM, N₂ adsorption isotherms, TG curves, additional XPS, Raman, additional XRD and TEM, additional CV and GCD curves, additional computational details, UV-vis, and performance comparison tables. See DOI: 10.1039/x0xx00000x

free charge carrier concentration.⁵² Several oxygen-deficient TiO₂ nanostructures with different polymorphs have been demonstrated to be able to deliver super rate capability for Li⁺/Na⁺/Mg²⁺ storage.⁵³⁻⁵⁷ Moreover, recent work also suggested that the introduction of sulfur or oxygen vacancies could improve the chemical interactions of the cathode hosts with polysulfides and enhanced the cycling stability of LSBs,^{30, 33, 58, 59} though the mechanism behind was still unclear.

Herein, we report oxygen-deficient TiO₂ as a cathode host for LSBs. Based on experimental observations and calculations by first-principles density functional theory (DFT), the V_o^{••} enhanced the affinity of TiO₂ towards polysulfides and simultaneously catalyzed their redox conversion by propelling the electron/Li⁺ transport on vacancy-enriched surface. As a result, the TiO₂/S composite cathode exhibited superior electrochemical performance. The presented methodology in this work may lead to new ideas on the design and exploration of novel nanocomposite electrodes with rationally engineered structural defects for next-generation electrochemical energy storage and conversion devices.

Results and Discussion



Scheme 1 Synthesis process of mesoporous oxygen-deficient TiO₂. (a) amorphous TiO₂/oleylamine hybrid, (b) mesoporous TiO₂ with minor oleylamine capping on surface, (c) mesoporous oxygen-deficient TiO₂ bonded with minor carbon, (d) mesoporous TiO₂.

The schematic fabrication procedure of mesoporous TiO₂ samples is shown in Scheme 1. First, amorphous TiO₂-oleylamine (TiO₂/OA) hybrid spheres were prepared by a sol-gel process (Scheme 1a). Then, the TiO₂/OA spheres were converted into mesoporous anatase TiO₂ spheres covered by trace OA by hydrothermal treatment in an ethanol/H₂O mixture (Scheme 1b). Finally, the mesoporous anatase TiO₂/OA spheres were annealed in Ar or air, leading to the formation of mesoporous oxygen-deficient anatase spheres (denoted as TiO₂-Ar, Scheme 1c) or oxygen vacancy-free anatase (TiO₂-air, Scheme 1d), respectively. Compared to white TiO₂-air, the TiO₂-Ar sample is in dark-brown colour (Fig. S1).

Scanning electron microscopy (SEM) images depict that both two samples consist of mesoporous spheres (1~2 μm in diameter) composed of connected particles of ~10 nm (Fig. S2). Such porous nanostructures possess high specific surface areas and pore volumes (118 m² g⁻¹ and 0.58 cm³ g⁻¹ for TiO₂-Ar; 121 m² g⁻¹ and 0.6 cm³ g⁻¹ for TiO₂-air), as determined by N₂ sorption isotherms using Brunauer-Emmett-Teller (BET) method (Fig. S3a and Table S1). The interconnection of nanocrystals yields

narrow pore distribution with sizes centering at 9.4 nm (for TiO₂-Ar) and 10.6 nm (for TiO₂-air) by Barrett-Joyner-Halenda (BJH) analyses (Fig. S4b).

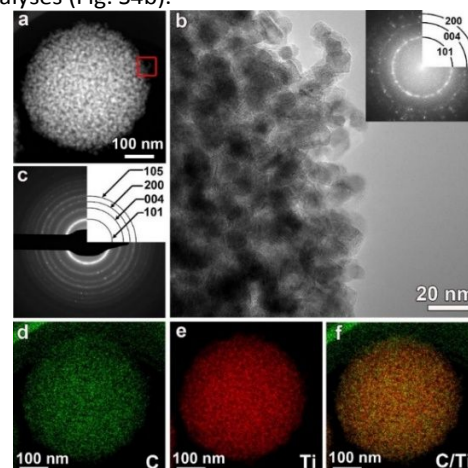


Fig. 1 TEM and EDX analysis of the TiO₂-Ar sample. (a) HAADF-STEM image; (b) HRTEM image of the area indicated by the red box in (a), (c) corresponding SAED pattern of the whole area in (a), (d-f) corresponding EDX elemental maps: C (green), Ti (red) and their overlay.

High-angle annular dark-field scanning transmission electron microscopy (HAADF-STEM) images (Fig. 1a) show that the TiO₂-Ar product contains mesoporous spheres comprised of crystalline nanoparticles. The corresponding selected area electron diffraction (SAED) (insets of Fig. 1b and c) presents the high degree of crystallinity of the TiO₂ nanoparticles. The high resolution TEM (HRTEM) image (Fig. 1b) reveals that most TiO₂ nanoparticles have clean surfaces, suggesting the low carbon content. The weight fraction of carbon has been further determined to be ~2wt% by thermogravimetric (TG) analyses (Fig. S4a). The corresponding energy-dispersive X-ray (EDX) elemental maps and overlay (Fig. 1d-f) validate that C and Ti are homogeneously distributed throughout the whole mesoporous sphere.

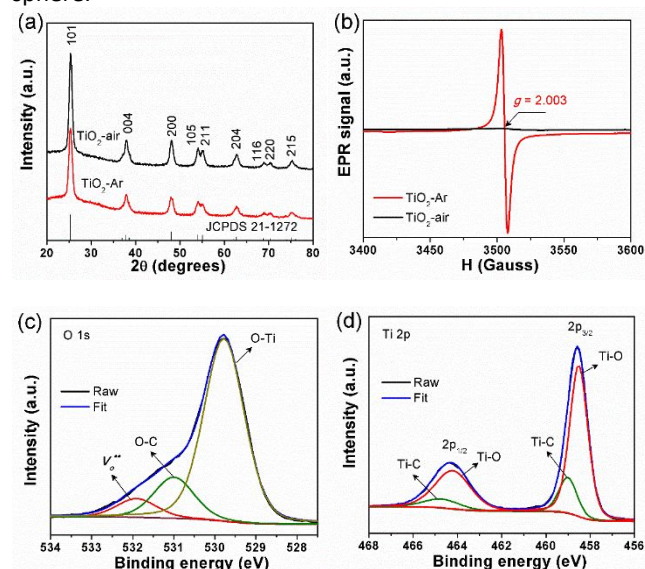


Fig. 2 (a) XRD patterns, (b) room-temperature EPR spectra of TiO₂-Ar and TiO₂-air samples; high-resolution XPS spectra of (c) O 1s and (d) Ti 2p in TiO₂-Ar/S sample.

To probe more structural information, X-ray diffraction (XRD), electron paramagnetic resonance (EPR), and X-ray photoelectron spectroscopy (XPS) and Raman characterizations were carried out. In Fig. 2a, XRD patterns of both samples can be readily indexed to anatase phase (space group $I4_1/amd$, JCPDS No. 21-1272) with good crystallinity.⁶⁰ Further, the XRD patterns indicate that TiO₂-Ar could have a smaller crystal size than that of TiO₂-air. It is very likely that the smaller grain size (thus highly exposed surface) of TiO₂-Ar can lead to a higher catalytic activity for polysulfide conversion when used in Li-S cells. In Fig. 2b, only one strong EPR signal with g value of ~ 2.003 is observed in the TiO₂-Ar, corresponding to the presence of $V_o^{\bullet\bullet}$ with excess electrons delocalized.^{56,57} The formation of $V_o^{\bullet\bullet}$ can be ascribed to the withdrawal of partial oxygen atoms from TiO₂ lattice during carbonization of residual oleyamine in Ar. In contrast, no EPR signal is detected in the TiO₂-air sample, implying either the absence or a very low $V_o^{\bullet\bullet}$ concentration. The deconvolution of O 1s XPS spectrum (Fig. 2c) reveals the presence of lattice O in TiO₂ (529.8 eV), O-C bonding (531 eV) and $V_o^{\bullet\bullet}$ at surface (532 eV).⁶¹ From the areal ratio of $V_o^{\bullet\bullet}$ versus lattice O, the concentration of oxygen vacancy on the surface can be estimated to be ca. 9%. In the deconvoluted Ti 2p XPS spectrum (Fig. 2d), two major bands with binding energy (BE) at 464.2 eV and 458.5 eV correspond well to the $2p_{1/2}$ and $2p_{3/2}$ components of Ti⁴⁺ in TiO₂ lattice.⁶² Two shoulder bands with higher BEs at 464.7 and 459 eV can be attributed to the Ti-C bond at TiO₂/C interface.^{56,63} The fitted C 1s spectrum (Fig. S5a) unravels the presence of sp^2 -hybridized C-C bonds (284.8 eV),⁶⁴ C-Ti bond (284.2 eV),⁶³ C-S bonds (285.5 eV),⁶² C-O (286.4 eV) and C=O bonds (288.7 eV).⁶⁵ S 2p XPS spectrum (Fig. S5b) indicates the existence of S-S bonds (164.71/163.55 eV) in orthorhombic S₈ molecules, S-C bonds (164.95/163.79 eV),⁶² and sulfate species from oxidation of surface sulfur (169.43/168.27 eV).⁶⁵ The formed Ti-C and C-S bonds at TiO₂/C and C/S interfaces can thus facilitate the electron transfer in the TiO₂-Ar/S electrode during electrochemical redox reactions. Raman measurements offer more local structural characteristics of the two samples. In Fig. S6, the Raman spectrum of TiO₂-air sample suggests its phase-pure anatase. Compared to TiO₂-air, the Raman peak intensity of TiO₂-Ar weakens greatly with several peaks almost diminished, suggesting the enhanced electric conduction enabled by $V_o^{\bullet\bullet}$ and carbon species because high conductivity could lower the skin depth of incident photons with reduced Raman scattering intensity.⁶⁶ In addition, two characteristic weak bands at 1387 and 1607 cm⁻¹ indicate the presence of amorphous carbon species.³⁸

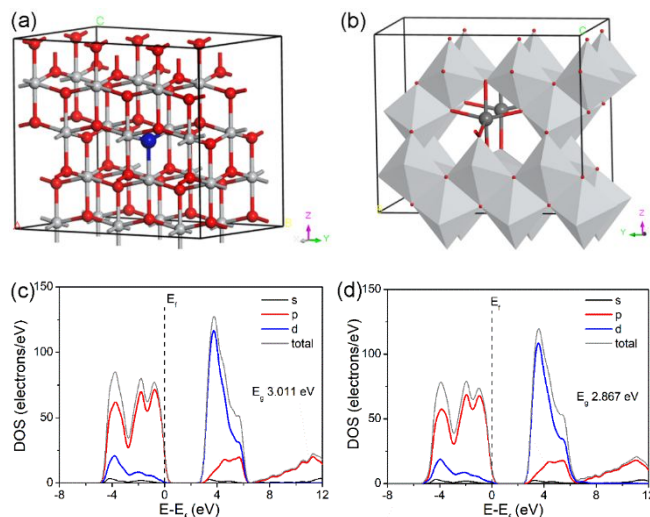


Fig. 3 Crystal and electronic structures of bulk TiO₂ after geometry optimization. (a) pristine anatase $2 \times 3 \times 1$ supercell shown in ball-and-stick mode (one O atom to be removed in (b) is labelled in blue), (b) anatase $2 \times 3 \times 1$ supercell with one $V_o^{\bullet\bullet}$ presented in polyhedral and ball-and-stick mode (the $V_o^{\bullet\bullet}$ is formed between two grey Ti atoms); (c, d) calculated total and partial density of states (DOS) of anatase $2 \times 3 \times 1$ supercells without (c) and with one $V_o^{\bullet\bullet}$ (d). The grey and red balls in (a, b) represent Ti and O atoms, respectively. E_f in (c, d) represents the Fermi energy level and its position is set at zero.

The influence of $V_o^{\bullet\bullet}$ on electronic structures of TiO₂ was further studied by first-principles density functional theory (DFT) calculations. Fig. 3a and b shows the optimized geometry structures of anatase supercell without and with $V_o^{\bullet\bullet}$, respectively. From the density of states (DOS) analyses, the electronic energy bandgap (E_g) of the TiO₂ supercell has been reduced from 3.011 eV to 2.867 eV after introducing $V_o^{\bullet\bullet}$, suggesting that $V_o^{\bullet\bullet}$ can enhance the electronic conductivity of TiO₂.^{55,57}

Next, sulfur was loaded into mesoporous TiO₂ by a conventional melt-diffusion approach. Compared to polar TiO₂, nonpolar carbon has a higher affinity to nonpolar sulfur as reflected by the smaller contact angle between carbon and melted sulfur (Fig. S7). Thus, it is deduced that the penetration of sulfur into TiO₂-Ar sample can be slightly easier than that of TiO₂-air due to the existence of trace nonpolar carbon in TiO₂-Ar. The resultant two composites (denoted as TiO₂-Ar/S and TiO₂-air/S, respectively) retain rough spherical morphologies albeit with the greatly reduced mesopores on surface (Fig. S8), leading to a sharp reduction of specific surface area (Fig. S3 and Table S1). XRD reveals that the loaded sulfur species in both two TiO₂ samples (Fig. S9) crystallize in orthorhombic phase (space group $Fddd$, JCPDS No. 42-1278).³³ TEM observation discloses that the defective structure (lattice distortion and $V_o^{\bullet\bullet}$) preserves after sulfur loading into TiO₂-Ar (Fig. S10).

The electrochemical properties of the resultant TiO₂/S composite electrodes in Li-S cells were evaluated using cyclic voltammetry (CV), galvanostatic charge/discharge (GCD) and electrochemical impedance spectroscopy (EIS) measurements. CV sweep of the TiO₂-Ar/S electrode (Fig. S11a) depicts that the TiO₂-Ar/S electrode undergoes a two-step reduction reaction during cathodic scan as suggested by two reduction peaks. The first peak at ~ 2.3 V corresponds to the reduction of solid S₈ to

long-chain soluble Li_2S_x ($4 \leq x \leq 8$), and the second at ~ 2.1 V represents further reduction from short-chain polysulfides to solid discharge product $\text{Li}_2\text{S}_2/\text{Li}_2\text{S}$.³⁰ In the following anodic sweep, only one merged oxidation peak appears at around 2.4 V, signifying the re-oxidation of $\text{Li}_2\text{S}/\text{Li}_2\text{S}_2$ to polysulfides and finally to solid sulfur.³⁰ The rough superimposition of the initial three CV cycles hints the high electrode reversibility with low loss of active sulfur species. GCD curves of $\text{TiO}_2\text{-Ar/S}$ electrode (Fig. S11b) also exhibit two discharge potential plateaus and one long charge plateau,³¹ which agrees with the CV data (Fig. S11a). In addition, the $\text{TiO}_2\text{-Ar/S}$ cathode delivers a high initial discharge capacity of 1578 mA h g^{-1} with a utilization of $\sim 94\%$ of the active sulfur species. The exact capacities from the upper-voltage plateau region and lower-voltage region are estimated to be ~ 401 and $\sim 1177 \text{ mA h g}^{-1}$, respectively. The small deviation of the GCD curves during first 3 cycles further demonstrates high reversibility.

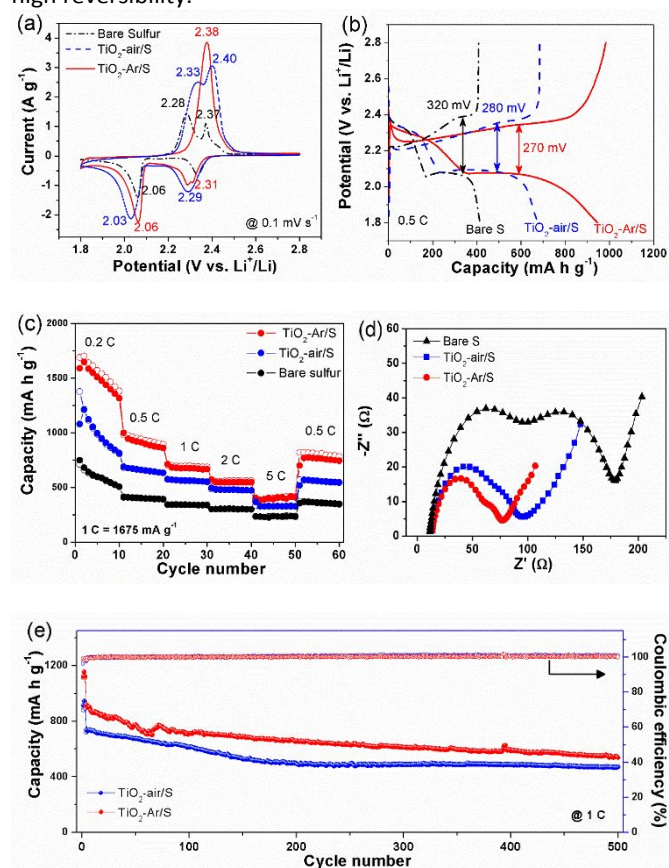


Fig. 4 Electrochemical performance of $\text{TiO}_2\text{-Ar/S}$, $\text{TiO}_2\text{-air/S}$ and bare sulfur electrodes. (a) cyclic voltammetry, (b) galvanostatic charge-discharge curves, (c) rate capability, (d) electrochemical impedance spectra, (e) long-term cyclability at 1 C (1675 mA g^{-1}).

For comparison, Fig. 4a compares the CV curves of the $\text{TiO}_2\text{-Ar/S}$, $\text{TiO}_2\text{-air/S}$ and bare sulfur electrodes. Clearly, $\text{TiO}_2\text{-Ar}$ exhibits much larger peak current response during the redox process and higher reduction peak position (~ 2.06 V) in the 2nd potential region, followed by a narrow and sharp oxidation peak, suggesting $\text{TiO}_2\text{-Ar}$ can effectively bind polysulfides and propel their conversion. In the GCD curves (Fig. 4b), both $\text{TiO}_2\text{-Ar/S}$ and $\text{TiO}_2\text{-air/S}$ (Fig. 4b) display a similar and lower

overpotential (~ 270 and 280 mV) than that of bare sulfur electrode (~ 320 mV) due to the enhanced reaction kinetics with reduced polarization.⁶⁷ In addition, $\text{TiO}_2\text{-Ar/S}$ cathode delivers the highest discharge capacity of 947 mA h g^{-1} , and the relative capacity contributions from the first upper-voltage and second lower-voltage regions are calculated to be 21% and 35.5%, respectively, higher than that of $\text{TiO}_2\text{-air/S}$ (14% and 26.5%) and pure sulfur (10.2% and 14.5%). The higher capacity of $\text{TiO}_2\text{-Ar/S}$ cathode mainly stems from the enhanced conductivity of the $\text{TiO}_2\text{-Ar}$ host with V_6O^{11} and carbon decoration.

Rate capability (Fig. 4c) displays that all the 3 electrodes manifest reduced capacities with increasing current rates from 0.2 to 5 C due to increased polarization. At 0.2 C, the two TiO_2/S electrodes exhibit a noticeable capacity drop. This phenomenon can be mainly caused by the existence of few sulfur species outside the mesoporous TiO_2 . Note that the pore volumes of our two samples are $\sim 0.6 \text{ cm}^3 \text{ g}^{-1}$, this value remains not very large compared to that of some porous carbon nanostructures ($>1 \text{ cm}^3 \text{ g}^{-1}$). Thus, few sulfur species could residue outside the TiO_2 surface. During discharge/charge, the outside sulfur species could form polysulfides and shuttle, giving rise to considerable capacity loss especially at low current density (e.g. 0.2 C). To solve this issue, it is necessary to further optimize the crystal size and particularly the pore structure (volume) of the mesoporous TiO_2 materials. In addition, additional modification of the surface of the mesoporous TiO_2 spheres, such as coating with highly conducting rGO nanosheets can also improve the cyclability and electronic conductivity of the composite cathode. Nonetheless, $\text{TiO}_2\text{-Ar/S}$ cathode can still sustain highly reversible capacities of 1591, 999, 712, 571 and 401 mA h g^{-1} at current densities of 0.2, 0.5, 1, 2 and 5 C, respectively. After switching the current rate back to 0.5 C, a capacity of 770 mA h g^{-1} was restored, demonstrating its good stability. In contrast, the $\text{TiO}_2\text{-air/S}$ electrode exhibits slightly inferior discharge capacities of 1081, 689, 576, 481 and 333 mA h g^{-1} at 0.2, 0.5, 1, 2 and 5 C, respectively. The pure sulfur electrode presents the poorest rate capacities of 711, 413, 341, and 234 mA h g^{-1} at 0.2, 0.5, 1, 2 and 5 C, respectively. The rate capability of the $\text{TiO}_2\text{-Ar/S}$ cathode also outperforms some reported sulfur hosts as summarized in Table S2 (Supporting Information). The electrode kinetics were further investigated by electrochemical impedance spectroscopy (EIS). As shown in Fig. 4d, the Nyquist plots of the three sulfur electrodes all contain two depressed semicircles at high and high-to-medium frequency regions as well as a sloping line at low frequency region. The first semicircle reflects the formation of a passivation film ($\text{Li}_2\text{S}_2/\text{Li}_2\text{S}$) on lithium anode surface and the second measures charge transfer resistance (R_{ct}) at cathode/electrolyte interface;³³ while the sloping line signifies the Li^+ diffusion in cathode. Apparently, the smallest R_{ct} of $\text{TiO}_2\text{-Ar/S}$ electrode compared to $\text{TiO}_2\text{-air/S}$ and bare sulfur cathode suggests the enhanced electronic/ionic conductivity in the $\text{TiO}_2\text{-Ar/S}$ electrode, faster charge transfer occurring at cathode/electrolyte interface and propelled polysulfide redox reactions.⁶⁷ The long-term cycling stability tests were also carried out at 0.2 C (Fig. S11c) and 1 C (Fig. 4e), respectively. At 0.2 C, the $\text{TiO}_2\text{-Ar/S}$ cathode shows a high initial discharge capacity of $\sim 1472 \text{ mA h g}^{-1}$ and retains 900

mA h g⁻¹ over 100 cycles with a retention rate of 61%, higher than those of the TiO₂-air/S (with an initial capacity of 1470 mA h g⁻¹ and retention rate of ~40%) and pristine sulfur (with an initial capacity 894 mA h g⁻¹ and retention rate of ~25%). Even at 1 C, the TiO₂-Ar/S electrode can manifest a high capacity of 538 mA h g⁻¹ over 500 cycles, higher than that of 467 mA h g⁻¹ for the TiO₂-air/S electrode. The cycling performance of the TiO₂-Ar/S cathode is also superior or comparable to recently reported cathode hosts for Li-S cells, as summarized in Table S3.

DFT calculations were applied to simulate the adsorption of polysulfide and Li, as well as Li diffusion on TiO₂ surface. Herein, Li₂S₄ was adopted as a representative polysulfide molecule and its adsorption on TiO₂ (100) surface was modelled. The simulation results reveal that the adsorption of Li₂S₄ on pristine anatase (100) yields a large binding energy (E_{ad}) of -3.95 eV. Note that the anatase (100) surface has rich two-coordinated O atoms and five-coordinated Ti atoms. After putting Li₂S₄ on the TiO₂ surface, one S atom from Li₂S₄ can bind with one five-coordinated Ti atom on the top surface, forming a S-Ti bond with a bond length of 2.447 Å (Fig. S12a). Meantime, the two Li atoms in Li₂S₄ can preferentially bind with their adjacent two-coordinated O atoms from TiO₂ surface, forming Li-O bonds with bond lengths ranging from 1.899 to 2.018 Å (Fig. S12a and b).

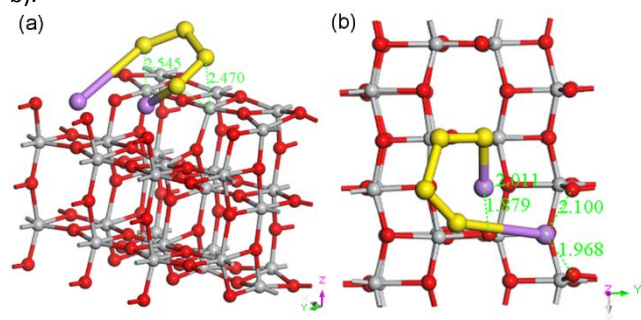


Fig. 5 (a) tilted and (b) top view of Li₂S₄ adsorbed on anatase (100) slab surface with V_{o}^{**} after geometry optimization, suggesting that its binding by S-Ti and Li-O bonds between Li₂S₄ and TiO₂. The grey, red, yellow, and pink balls represent Ti, O, S, and Li, respectively.

In comparison, the adsorption of Li₂S₄ on TiO₂ surface with V_{o}^{**} has two preferential configurations after geometry optimization. In the first one (Fig. S12c and d), the two Li atoms tend to coordinate with their adjacent O atoms on TiO₂ surface to form Li-O bonding; while the one S atom prefers to bind with a four-coordinated Ti atom (adjacent to V_{o}^{**}), showing an increased covalent characteristic with shorter bond length (2.313 Å) and higher E_{ad} (-4.84 eV) (Fig. S12c). The formation of multiple Li-O bonds and one S-Ti bonds at Li₂S₄/TiO₂ (100) surface containing V_{o}^{**} has been further elucidated by the charge density difference plots (Fig. S13a). In the second configuration, we interestingly notice that the on-top four-coordinated Ti atom (surrounding V_{o}^{**}) can also simultaneously bind two S atoms and a five-coordinated Ti binds another S from Li₂S₄, leading to even stronger chemical adsorption (E_{ad} of -5.23 eV), as shown in Fig. 5 and S12b. Our calculated E_{ad} values of polysulfide on TiO₂ (100) with and without V_{o}^{**} are both higher than or comparable to some reported polar host materials, such

as Ni₂P (-3.7 eV) and Co₂P (-4.18 eV),⁴² N-doped graphene (-3.11 eV),⁶⁸ and Li_xTiS₂ (-3.4~4 eV),⁶⁹ suggesting that polysulfide can be tightly adsorbed on the TiO₂ surface via interfacial chemical bonding.

The high affinity of the TiO₂ toward polysulfide with reduced shuttling effect has been further validated by visual adsorption experiments and ultraviolet-visible (UV-vis) spectra (Fig. S14) as well as post-mortem analyses of the Li-S cell components (Fig. S15). In addition, one Li-S bond in Li₂S₄ adsorbed both on anatase (100) and TiO₂ (100) with V_{o}^{**} has been significantly elongated and breaks due to the strong coordination of Li with multiple surface O atoms, suggesting that the adsorbed Li₂S₄ tends to further decompose into lower-order polysulfide. Given that the high electric conductivity of the TiO₂-Ar promoted by V_{o}^{**} and Ti-C bonding, the adsorbed Li₂S₄ on TiO₂-Ar surface is expected to decompose spontaneously and quickly,⁷⁰ leading to fast conversion kinetics.

To evaluate the redox kinetics of surface-adsorbed polysulfide species, the Li adsorption on TiO₂ (100) surface was also investigated. The results indicate that one preferential position for Li adsorption locates near to the trigonal centre of 3 adjacent O atoms (Fig. S16a and b). Such configuration of Li adsorption via coordination with three O atoms gives a large E_{ad} of -4.43 eV. In contrast, the Li adsorption on the surface with V_{o}^{**} is similar to that of pristine (100) surface, except that a subtle deviation of the trigonal centre possibly due to the lack of one coordinated O atom at the V_{o}^{**} position (Fig. S16c and d). This also yields an E_{ad} of -3.63 eV. These large E_{ad} values of Li ion adsorption on TiO₂ surface (without/with V_{o}^{**}) suggest that Li can be concentrated on the TiO₂ (100) surface,⁷¹ participating in fast redox reaction of polysulfides during charge/discharge.

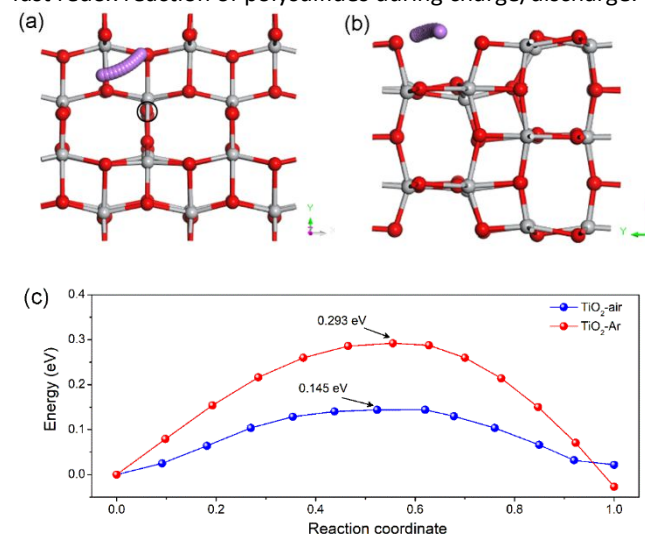


Fig. 6 Top (a) and side view (b) of Li diffusion on anatase (100) slab surface and corresponding energy profiles (c). The grey, red, and pink balls represent the Ti, O, and Li, respectively. The black circle in (a) signifies the V_{o}^{**} position.

Next, the influence of V_{o}^{**} on the Li ion diffusion on TiO₂ surface was further simulated. The calculated Li ion diffusion pathways on pristine anatase (100) surface and surface with V_{o}^{**} are shown in Fig. S17 and Fig. 6, respectively. It depicts that Li ion can transport easily on TiO₂ surface with a very low energy

barrier of 0.145 eV (Fig. 6c). In comparison, the presence of V_o^{**} slightly impedes the Li ion diffusion surrounding V_o^{**} affinity possibly due to the enhanced scattering of positively charged V_o^{**} towards Li ions. However, this value (0.293 eV) is smaller than that in some oxides and sulfides, such as SnO_2 (~1.0 eV) and MoS_2 (~0.8 eV),⁷² and Sb_2S_3 nanosheets (~0.31 eV).⁷³ The combined large electronic conductivity, high concentration of Li ions on TiO_2 surface with large diffusivity ensure fast electrochemical redox conversion of polysulfides with fast kinetics,^{67,72,73} which agree well with electrochemical properties/performances shown in Fig. 4.

Conclusions

Oxygen-deficient TiO_2 has been successfully synthesized by a facile hydrothermal process combined with post annealing in Ar. Experimental data and DFT theoretical simulations reveal that the formation of oxygen vacancy (V_o^{**}) effectively improves the electrical conduction in TiO_2 and enhances the binding of TiO_2 surface to polysulfides. Meantime, Li ions can be concentrated and diffuse easily on the oxygen-deficient TiO_2 surface, propelling fast redox conversion kinetics of surface adsorbed polysulfides. When evaluated in Li-S cells, the TiO_2/S composite cathode delivers high capacity, outstanding rate and excellent cycling stability. The proposed vacancy engineering approach may pave the way for rational design of novel sulfur host materials for high-performance Li-S batteries.

Conflicts of interest

There are no conflicts to declare.

Acknowledgements

This work is financially supported by the Basic Research Project of the Science and Technology Innovation Commission of Shenzhen (No. JCYJ20170817110251498), the Guangdong Special Support for the Science and Technology Leading Young Scientist (No. 2016TQ03C919), National Natural Science Foundation of China (51672230, 21603094), General Research Fund (GRF CityU 11338516), and in part by the National Science Foundation (No. 1803256). H.-E. Wang acknowledges Hubei Provincial Department of Education for the "Chutian Scholar" program.

Notes and references

1. Q. Pang, X. Liang, C. Y. Kwok and L. F. Nazar, *Nat. Energy*, 2016, **1**, 16132.
2. Y.-X. Yin, S. Xin, Y.-G. Guo and L.-J. Wan, *Angew. Chem. Int. Ed.*, 2013, **52**, 13186-13200.
3. A. Manthiram, Y. Fu and Y.-S. Su, *Acc. Chem. Res.*, 2013, **46**, 1125-1134.
4. G. Li, S. Wang, Y. Zhang, M. Li, Z. Chen and J. Lu, *Adv. Mater.*, 2018, **30**, 1705590.
5. J. Sun, Y. Sun, M. Pasta, G. Zhou, Y. Li, W. Liu, F. Xiong and Y. Cui, *Adv. Mater.*, 2016, **28**, 9797-9803.
6. J. Park, B.-C. Yu, J. S. Park, J. W. Choi, C. Kim, Y.-E. Sung and J. B. Goodenough, *Adv. Energy Mater.*, 2017, **7**, 1602567.
7. Y.-S. Su and A. Manthiram, *Nat. Commun.*, 2012, **3**, 1166.
8. J. Liu, M. Sun, Q. Zhang, F. Dong, P. Kaghazchi, Y. Fang, S. Zhang and Z. Lin, *J. Mater. Chem. A*, 2018, **6**, 7382-7388.
9. G. Xu, Q.-b. Yan, A. Kushima, X. Zhang, J. Pan and J. Li, *Nano Energy*, 2017, **31**, 568-574.
10. W. Chen, T. Lei, C. Wu, M. Deng, C. Gong, K. Hu, Y. Ma, L. Dai, W. Lv, W. He, X. Liu, J. Xiong and C. Yan, *Adv. Energy Mater.*, 2018, **8**, 1702348.
11. S. Y. Lang, R. J. Xiao, L. Gu, Y. G. Guo, R. Wen and L. J. Wan, *J. Am. Chem. Soc.*, 2018, **140**, 8147-8155.
12. S. Wu, Z. Zhang, M. Lan, S. Yang, J. Cheng, J. Cai, J. Shen, Y. Zhu, K. Zhang and W. Zhang, *Adv. Mater.*, 2018, **30**, 1705830.
13. J. Xu, T. Lawson, H. Fan, D. Su and G. Wang, *Adv. Energy Mater.*, 2018, **8**, 1702607.
14. J. Park, S.-H. Yu and Y.-E. Sung, *Nano Today*, 2018, **18**, 35-64.
15. S. Rehman, K. Khan, Y. Zhao and Y. Hou, *J. Mater. Chem. A*, 2017, **5**, 3014-3038.
16. X. Ji, K. T. Lee and L. F. Nazar, *Nat. Mater.*, 2009, **8**, 500-506.
17. X. Li, Y. Cao, W. Qi, L. V. Saraf, J. Xiao, Z. Nie, J. Mietek, J.-G. Zhang, B. Schwenzer and J. Liu, *J. Mater. Chem.*, 2011, **21**, 16603-16610.
18. N. Jayaprakash, J. Shen, S. S. Moganty, A. Corona and L. A. Archer, *Angew. Chem. Int. Ed.*, 2011, **50**, 5904-5908.
19. F. Pei, T. An, J. Zang, X. Zhao, X. Fang, M. Zheng, Q. Dong and N. Zheng, *Adv. Energy Mater.*, 2016, **6**, 1502539.
20. (a) J. Cao, C. Chen, Q. Zhao, N. Zhang, Q. Lu, X. Wang, Z. Niu and J. Chen, *Adv. Mater.*, 2016, **28**, 9629; (b) X. Wang, Y. Li, T. Jin, J. Meng, L. Jiao, M. Zhu and J. Chen, *Nano Lett.*, 2017, **17**, 7989-7994; (c) X. J. Wang, K. Z. Cao, Y. J. Wang and L. F. Jiao, *Small*, 2017, **13**, 1700873.
21. M. Yan, H. Chen, Y. Yu, H. Zhao, C. F. Li, Z. Y. Hu, P. Wu, L. H. Chen, H. E. Wang, D. L. Peng, H. X. Gao, T. Hasan, Y. Li and B. L. Su, *Adv. Energy Mater.*, 2018, **8**, 1801066.
22. C. Tang, B. Q. Li, Q. Zhang, L. Zhu, H. F. Wang, J. L. Shi and F. Wei, *Adv. Funct. Mater.*, 2016, **26**, 577-585.
23. J. Zhang, C. P. Yang, Y. X. Yin, L. J. Wan and Y. G. Guo, *Adv. Mater.*, 2016, **28**, 9539.
24. Z.-L. Xu, J.-K. Kim and K. Kang, *Nano Today*, 2018, **19**, 84-107.
25. Z. B. Cheng, H. Pan, H. Zhong, Z. B. Xiao, X. J. Li and R. H. Wang, *Adv. Funct. Mater.*, 2018, **28**, 1707597.
26. X. Liang and L. F. Nazar, *ACS Nano*, 2016, **10**, 4192-4198.
27. X. Y. Tao, J. G. Wang, Z. G. Ying, Q. X. Cai, G. Y. Zheng, Y. P. Gan, H. Huang, Y. Xia, C. Liang, W. K. Zhang and Y. Cui, *Nano Lett.*, 2014, **14**, 5288-5294.
28. H. E. Wang, K. L. Yin, X. Zhao, N. Qin, Y. Li, Z. Deng, L. C. Zheng, B. L. Su and Z. G. Lu, *Chem. Commun.*, 2018, **54**, 12250-12253.
29. U. Zubair, J. Amici, C. Francia, D. McNulty, S. Bodoardo and C. O'Dwyer, *ChemSusChem*, 2018, **11**, 1838-1848.
30. Y. Zhang, Z. Mu, C. Yang, Z. Xu, S. Zhang, X. Zhang, Y. Li, J. Lai, Z. Sun, Y. Yang, Y. Chao, C. Li, X. Ge, W. Yang and S. Guo, *Adv. Funct. Mater.*, 2018, **28**, 1707578.
31. Z. B. Cheng, Z. B. Xiao, H. Pan, S. Q. Wang and R. H.

- Wang, *Adv. Energy Mater.*, 2018, **8**, 1702337.
32. S. Z. Huang, Y. Wang, J. P. Hu, Y. V. Lim, D. Z. Kong, Y. Zheng, M. Ding, M. E. Pam and H. Y. Yang, *ACS Nano*, 2018, **12**, 9504-9512.
33. X. C. Li, G. L. Guo, N. Qin, Z. Deng, Z. G. Lu, D. Shen, X. Zhao, Y. Li, B. L. Su and H. E. Wang, *Nanoscale*, 2018, **10**, 15505-15512.
34. C. Y. Fan, Y. P. Zheng, X. H. Zhang, Y. H. Shi, S. Y. Liu, H. C. Wang, X. L. Wu, H. Z. Sun and J. P. Zhang, *Adv. Energy Mater.*, 2018, **8**, 1703638.
35. C. Shang, L. Cao, M. Yang, Z. Wang, M. Li, G. Zhou, X. Wang and Z. Lu, *Energy Storage Mater.*, 2018, 10.1016/j.ensm.2018.1008.1013.
36. L. B. Ma, H. Yuan, W. J. Zhang, G. Y. Zhu, Y. R. Wang, Y. Hu, P. Y. Zhao, R. P. Chen, T. Chen, J. Liu, Z. Hu and Z. Jin, *Nano Lett.*, 2017, **17**, 7839-7846.
37. Y. Z. Song, W. Zhao, L. Kong, L. Zhang, X. Y. Zhu, Y. L. Shao, F. Ding, Q. Zhang, J. Y. Sun and Z. F. Liu, *Energy Environ. Sci.*, 2018, **11**, 2620-2630.
38. Y. Zhong, D. L. Chao, S. J. Deng, J. Y. Zhan, R. Y. Fang, Y. Xia, Y. D. Wang, X. L. Wang, X. H. Xia and J. P. Tu, *Adv. Funct. Mater.*, 2018, **28**, 1706391.
39. X. X. Li, K. Ding, B. Gao, Q. W. Li, Y. Y. Li, J. J. Fu, X. M. Zhang, P. K. Chu and K. F. Huo, *Nano Energy*, 2017, **40**, 655-662.
40. Z. H. Li, Q. He, X. Xu, Y. Zhao, X. W. Liu, C. Zhou, D. Ai, L. X. Xia and L. Q. Mai, *Adv. Mater.*, 2018, **30**, 1804089.
41. C. Ye, Y. Jiao, H. Jin, A. D. Slattery, K. Davey, H. Wang and S.-Z. Qiao, *Angew. Chem. Int. Ed.*, 2018, 30325094.
42. H. Yuan, X. Chen, G. Zhou, W. Zhang, J. Luo, H. Huang, Y. Gan, C. Liang, Y. Xia, J. Zhang, J. Wang and X. Tao, *ACS Energy Lett.*, 2017, **2**, 1711-1719.
43. S. Z. Huang, Y. V. Lim, X. M. Zhang, Y. Wang, Y. Zheng, D. Z. Kong, M. Ding, S. Y. A. Yang and H. Y. Yang, *Nano Energy*, 2018, **51**, 340-348.
44. Z. W. Seh, W. Li, J. J. Cha, G. Zheng, Y. Yang, M. T. McDowell, P.-C. Hsu and Y. Cui, *Nat. Commun.*, 2013, **4**, 1331.
45. S. Evers, T. Yim and L. F. Nazar, *J. Phys. Chem. C*, 2012, **116**, 19653-19658.
46. G. Xu, Q.-b. Yan, S. Wang, A. Kushima, P. Bai, K. Liu, X. Zhang, Z. Tang and J. Li, *Chem. Sci.*, 2017, **8**, 6619-6625.
47. Y. Y. Li, Q. F. Cai, L. Wang, Q. W. Li, X. Peng, B. Gao, K. F. Huo and P. K. Chu, *ACS Appl. Mater. Interfaces*, 2016, **8**, 23784-23792.
48. M. Yu, J. Ma, H. Song, A. Wang, F. Tian, Y. Wang, H. Qiu and R. Wang, *Energy Environ. Sci.*, 2016, **9**, 1495-1503.
49. J.-Y. Hwang, H. M. Kim, S.-K. Lee, J.-H. Lee, A. Abouimrane, M. A. Khaleel, I. Belharouak, A. Manthiram and Y.-K. Sun, *Adv. Energy Mater.*, 2016, **6**, 1501480.
50. W. L. Wu, J. Pu, J. Wang, Z. H. Shen, H. Y. Tang, Z. T. Deng, X. Y. Tao, F. Pan and H. G. Zhang, *Adv. Energy Mater.*, 2018, **8**, 1702373.
51. X. T. Gao, Y. Xie, X. D. Zhu, K. N. Sun, X. M. Xie, Y. T. Liu, J. Y. Yu and B. Ding, *Small*, 2018, **14**, 1802443.
52. Z. Liang, G. Y. Zheng, W. Y. Li, Z. W. Seh, H. B. Yao, K. Yan, D. S. Kong and Y. Cui, *ACS Nano*, 2014, **8**, 5249-5256.
53. T. Xia, W. Zhang, J. B. Murowchick, G. Liu and X. B. Chen, *Adv. Energy Mater.*, 2013, **3**, 1516-1523.
54. Y. Wu, Y. Jiang, J. Shi, L. Gu and Y. Yu, *Small*, 2017, **13**, 1700129.
55. Y. Zhang, Z. Y. Ding, C. W. Foster, C. E. Banks, X. Q. Qiu and X. B. Ji, *Adv. Funct. Mater.*, 2017, **27**, 1700856.
56. C. Zhao, Y. Cai, K. Yin, H. Li, D. Shen, N. Qin, Z. Lu, C. Liu and H.-E. Wang, *Chem. Eng. J.*, 2018, **350**, 201-208.
57. Y. Wang, X. Xue, P. Liu, C. Wang, X. Yi, Y. Hu, L. Ma, G. Zhu, R. Chen, T. Chen, J. Ma, J. Liu and Z. Jin, *ACS Nano*, 2018, **12**, 12492-12502.
58. L. Kong, X. Chen, B. Q. Li, H. J. Peng, J. Q. Huang, J. Xie and Q. Zhang, *Adv. Mater.*, 2018, **30**, 1705219.
59. H. C. Wang, C. Y. Fan, Y. P. Zheng, X. H. Zhang, W. H. Li, S. Y. Liu, H. Z. Sun, J. P. Zhang, L. N. Sun and X. L. Wu, *Chem. Eur. J.*, 2017, **23**, 9666-9673.
60. Y. Cai, H. E. Wang, S. Z. Huang, M. F. Yuen, H. H. Cai, C. Wang, Y. Yu, Y. Li, W. J. Zhang and B. L. Su, *Electrochim. Acta*, 2016, **210**, 206-214.
61. J. Chen, Z. Ding, C. Wang, H. Hou, Y. Zhang, C. Wang, G. Zou and X. Ji, *ACS Appl. Mater. Interfaces*, 2016, **8**, 9142-9151.
62. H.-E. Wang, X. Zhao, X. Li, Z. Wang, C. Liu, Z. Lu, W. Zhang and G. Cao, *J. Mater. Chem. A*, 2017, **5**, 25056-25063.
63. Y. Cai, H. E. Wang, X. Zhao, F. Huang, C. Wang, Z. Deng, Y. Li, G. Z. Cao and B. L. Su, *ACS Appl. Mater. Interfaces*, 2017, **9**, 10652-10663.
64. H.-E. Wang, X. Zhao, K. Yin, Y. Li, L. Chen, X. Yang, W. Zhang, B.-L. Su and G. Cao, *ACS Appl. Mater. Interfaces*, 2017, **9**, 43665-43673.
65. C. Zheng, S. Niu, W. Lv, G. Zhou, J. Li, S. Fan, Y. Deng, Z. Pan, B. Li, F. Kang and Q.-H. Yang, *Nano Energy*, 2017, **33**, 306-312.
66. M. Ben Yahia, F. Lemoigno, T. Beuvier, J.-S. Filhol, M. Richard-Plouet, L. Brohan and M.-L. Doublet, *J. Chem. Phys.*, 2009, **130**, 204501.
67. M. Wang, L. Fan, D. Tian, X. Wu, Y. Qiu, C. Zhao, B. Guan, Y. Wang, N. Zhang and K. sun, *ACS Energy Lett.*, 2018, **3**, 1627-1633.
68. L.-C. Yin, J. Liang, G.-M. Zhou, F. Li, R. Saito and H.-M. Cheng, *Nano Energy*, 2016, **25**, 203-210.
69. X.-C. Liu, Y. Yang, J. Wu, M. Liu, S. P. Zhou, B. D. A. Levi, X.-D. Zhou, H. Cong, D. A. Muller, P. M. Ajayan, H. D. Abruna and F.-S. Ke, *ACS Energy Lett.*, 2018, **3**, 1325-1330.
70. F. X. Wu, T. P. Pollard, E. B. Zhao, Y. R. Xiao, M. Olguin, O. Borodin and G. Yushin, *Energy Environ. Sci.*, 2018, **11**, 807-817.
71. G. Y. Xu, Q. B. Yan, S. T. Wang, A. Kushima, P. Bai, K. Liu, X. G. Zhang, Z. L. Tang and J. Li, *Chem. Sci.*, 2017, **8**, 6619-6625.
72. G. Zhou, H. Tian, Y. Jin, X. Tao, B. Liu, R. Zhang, Z. W. Seh, D. Zhuo, Y. Liu, J. Sun, J. Zhao, C. Zu, D. S. Wu, Q. Zhang and Y. Cui, *Proc. Nat. Aca. Sci.*, 2017, **114**, 840-845.
73. S. Yao, J. Cui, J.-Q. Huang, Z. Lu, Y. Deng, W. G. Chong, J. Wu, M. I. U. Haq, F. Ciucci and J.-K. Kim, *Adv. Energy Mater.*, 2018, **8**, 1800710.